

A Learnable Variational Model for Joint Multimodal MRI Reconstruction and Synthesis

Wanyu Bian¹, Qingchao Zhang¹, Xiaojing Ye², and Yunmei Chen¹

¹ University of Florida, Gainesville FL 32611, USA
 {wanyu.bian, qingchaozhang, yun}@ufl.edu

² Georgia State University, Atlanta GA 30302, USA
 xye@gsu.edu

Abstract. Generating multi-contrasts/modal MRI of the same anatomy enriches diagnostic information but is limited in practice due to excessive data acquisition time. In this paper, we propose a novel deep-learning model for joint reconstruction and synthesis of multi-modal MRI using incomplete k-space data of several source modalities as inputs. The output of our model includes reconstructed images of the source modalities and high-quality image synthesized in the target modality. Our proposed model is formulated as a variational problem that leverages several learnable modality-specific feature extractors and a multimodal synthesis module. We propose a learnable optimization algorithm to solve this model, which induces a multi-phase network whose parameters can be trained using multi-modal MRI data. Moreover, a bilevel-optimization framework is employed for robust parameter training. We demonstrate the effectiveness of our approach using extensive numerical experiments.

Keywords: MRI Reconstruction · Multimodal MRI Synthesis · Deep Neural Network · Bilevel-Optimization.

1 Introduction

Magnetic resonance imaging (MRI) is a prominent leading-edge medical imaging technology which provides diverse image contrasts under the same anatomy. Multiple different contrast images are generated by varying the acquisition parameters, e.g. T1-weighted (T1), T2-weighted (T2) and Fluid Attenuated Inversion Recovery (FLAIR). They have similar anatomical structure but highlight different soft tissue which enriches the diagnostic information for clinical applications and research studies comparing to single modality [10]. A major limitation of MRI is its relatively long data acquisition time during MRI scans. It does not only cause patient discomfort, but also makes MR images prone to motion artifacts which degrade the diagnostic accessibility. A mainstream routine to reduce the MRI acquisition time is to reconstruct partially undersampled k-space acquisitions, another approach is to synthesize target modality MR image from fully-sampled acquisitions of source modality images [24,7].

Compressed sensing MRI (CS-MRI) reconstruction is a predominant approach for accelerating MR acquisitions, which solves an inverse problem formulated as a

variational model. In recent decades, deep learning based models have leveraged large datasets and further explored the potential improvement of reconstruction performance. Most of the deep learning based reconstruction methods employ end-to-end deep networks [23,19,11]. To overcome the weakness of the end-to-end black-box networks, several learnable optimization algorithms (LOAs) have been developed attracted much attention, which possess of a more interpretable network architecture. LOA-based reconstruction methods unfold the iterative optimization algorithm into a multi-phase network in which the regularization and image transformation are learned to improve the network performance [15,2,4,1], e.g. ADMM-Net [20], ISTA-Net⁺ [26] and PD-Net [5].

MR image synthesis in recent years has emerged using various deep learning frameworks, which can be roughly categorized into unimodal synthesis [6,18,22] and multimodal synthesis [3,7,17,25]. Unimodal synthesis is an one-to-one approach that aims to generate images of a target modality from the corresponding single source modality. A common deep learning based strategy is adversarial method such as pGAN [6], which minimizes the adversarial loss to capture reliable high-frequency texture information. Multimodal synthesis is a many-to-one or many-to-many type of approach, most of which use the GAN-based network and their networks are mostly end-to-end with encoder-decoder architectures, especially the generator networks of adversarial learning. For example, MM-GAN [17] concatenates all the available modalities channel-wisely with a zero image as missing modality and imputes the missing input incorporating curriculum learning for GAN. Multimodal MR (MM) [12], MMGradAdv [3] and Hi-Net [27] exploit the correlations among multimodal data and apply robust feature fusion method to form a unified latent representation.

In order to synthesize target modality by using partially scanned k-space data from source modalities in stead of fully scanned data that used in the state-of-the-art multimodal synthesis, in this paper, we propose to jointly reconstruct undersampled multiple source modality MR images and synthesize the target modality image. Our contributions are summarized as follows: (1) We propose a novel LOA for joint multimodal MRI reconstruction and synthesis with theoretical analysis guarantee; (2) The parameters and hyper-parameters of the network induced by our LOA are learned using a bilevel optimization algorithm robust parameter training; (3) Extensive experimental results demonstrate the efficiency of the proposed method and high quality of the reconstructed/synthesized images.

2 Proposed Method

2.1 Model

In this section, we provide the details of the proposed model for joint MRI reconstruction and synthesis. Given the partial k-space data $\{\mathbf{f}_1, \mathbf{f}_2\}$ of the source modalities (e.g. T1 and T2), our goal is to reconstruct the corresponding images $\{\mathbf{x}_1, \mathbf{x}_2\}$ and synthesize the image \mathbf{x}_3 of the missing modality (e.g. FLAIR) without its k-space data. To this end, we propose to learn three modality-specific feature extraction operators $\{h_{w_i}\}_{i=1}^3$, one for each of these three modalities.

Then, we design regularizers of these images by combining these learned operators and a robust sparse feature selection operator (we use $(2, 1)$ -norm in this work). To synthesize the image \mathbf{x}_3 using \mathbf{x}_1 and \mathbf{x}_2 , we employ another feature-fusion operator g_θ which learns the mapping from the features $h_{w_1}(\mathbf{x}_1)$ and $h_{w_2}(\mathbf{x}_2)$ to the image \mathbf{x}_3 . Our proposed model reads as

$$\begin{aligned} \min_{\mathbf{x}_1, \mathbf{x}_2, \mathbf{x}_3} \Psi_{\Theta, \gamma}(\mathbf{x}_1, \mathbf{x}_2, \mathbf{x}_3) := & \frac{1}{2} \sum_{i=1}^2 \|P_i F \mathbf{x}_i - \mathbf{f}_i\|_2^2 + \frac{1}{3} \sum_{i=1}^3 \|h_{w_i}(\mathbf{x}_i)\|_{2,1} \\ & + \frac{\gamma}{2} \|g_\theta([h_{w_1}(\mathbf{x}_1), h_{w_2}(\mathbf{x}_2)]) - \mathbf{x}_3\|_2^2, \end{aligned} \quad (1)$$

where the first term in (1) is the data fidelity for the source modalities that ensures consistency between the reconstructed images $\{\mathbf{x}_1, \mathbf{x}_2\}$ and the sensed partial k-space data $\{\mathbf{f}_1, \mathbf{f}_2\}$. Here, F stands for the discrete Fourier transform and P_i is the binary matrix representing the k-space mask when acquiring data for \mathbf{x}_i . In (1), h_{w_i} represents the modality-specific feature extraction operator which maps the input $\mathbf{x}_i \in \mathbb{C}^n$ to a high-dimensional feature tensor $h_{w_i}(\mathbf{x}_i) \in \mathbb{C}^{m \times d}$, where m is the spatial dimension and d is the channel number of the feature tensor. The second term is the regularization of all modalities $\{\mathbf{x}_1, \mathbf{x}_2, \mathbf{x}_3\}$ to enhance sparsity of their feature tensors, where $\|h_{w_i}(\mathbf{x}_i)\|_{2,1} = \sum_{j=1}^m \|h_{w_i,j}(\mathbf{x}_i)\|$. Here each $h_{w_i,j} \in \mathbb{R}^d$ can be viewed as a feature vector at spatial location j . The last term in (1) is to synthesize \mathbf{x}_3 by learning a mapping $g_\theta : \mathbb{C}^{m \times 2d} \rightarrow \mathbb{C}^n$ that maps the concatenated features of \mathbf{x}_1 and \mathbf{x}_2 (i.e. $[h_{w_1}(\mathbf{x}_1), h_{w_2}(\mathbf{x}_2)]$) to \mathbf{x}_3 , and $[\cdot, \cdot]$ represents the concatenation of the arguments.

In our implementation, we parameterize the modality-specific feature extraction operator h_{w_i} and the synthesis mapping g_θ as vanilla CNNs with l and l' layers respectively, both of which use the smoothed rectified linear unit [4] as activation. For notation simplicity, we let Θ in (1) denote the collection of all parameters in the convolution operators of the function Ψ , i.e. $\Theta = \{w_1, w_2, w_3, \theta\}$.

The weight γ is a hyper-parameter which plays a critical role in balancing the reconstruction part (first two terms in (1)) and the image synthesis part (last term in (1)) of the model (1), and hence has significant impact to the final image reconstruction and synthesis quality. To address this important issue, we propose to use a bi-level hyper-parameter tuning framework to learn γ by minimizing the reconstruction loss on both validation and training data sets. Details of this hyper-parameter tuning will be provided in Section 2.3.

2.2 Efficient Learnable Optimization Algorithm

In this section, we present a novel and efficient learnable optimization algorithm (LOA) for solving the nonconvex nonsmooth minimization problem (1). (Comprehensive convergence analysis of this algorithm is provided in Supplementary Material.) Then we design a DNN whose architecture exactly follows this algorithm, and the parameters of the DNN can be learned from data. In this way, the DNN inherits all the convergence properties of the LOA.

Since the second sum in the minimization problem (1) is nonsmooth due to the $l_{2,1}$ -norm, we first approximate these nonsmooth terms using their smooth

Algorithm 1: Learnable Descent Algorithm

```

1: Input:  $\mathbf{X}^{(0)}$ ,  $0 < \eta < 1$ , and  $\varepsilon_0, a, \sigma > 0$ ,  $t = 0$ . Max  $T$ , tolerance  $\epsilon_{\text{tol}} > 0$ .
2: for  $t = 0, 1, 2, \dots, T - 1$  do
3:    $\mathbf{X}^{(t+1)} = \mathbf{X}^{(t)} - \alpha_t \nabla \Psi_{\Theta, \gamma}^{\varepsilon_t}(\mathbf{X}^{(t)})$ , where the step size  $\alpha_t$  is obtained through
      line search s.t.  $\Psi_{\Theta, \gamma}^{\varepsilon_t}(\mathbf{X}^{(t+1)}) - \Psi_{\Theta, \gamma}^{\varepsilon_t}(\mathbf{X}^{(t)}) \leq -\frac{1}{a} \|\mathbf{X}^{(t+1)} - \mathbf{X}^{(t)}\|^2$  holds.
4:   if  $\|\nabla \Psi_{\Theta, \gamma}^{\varepsilon_t}(\mathbf{X}^{(t+1)})\| < \sigma \eta \varepsilon_t$ , set  $\varepsilon_{t+1} = \eta \varepsilon_t$ ; otherwise, set  $\varepsilon_{t+1} = \varepsilon_t$ .
5:   if  $\sigma \varepsilon_t < \epsilon_{\text{tol}}$ , terminate and go to Line 6,
6: end for and output  $\mathbf{X}^{(t)}$ .

```

surrogates $\|h_{w_i}(\mathbf{x}_i)\|_{\varepsilon_{2,1}} = \sum_{j=1}^m (\sqrt{\|h_{w_i,j}(\mathbf{x}_i)\|^2 + \varepsilon^2} - \varepsilon)$, where $\varepsilon > 0$ is the parameter representing the smoothing level. Thus, for every fixed ε , we obtain a smooth surrogate function $\Psi_{\Theta, \gamma}^{\varepsilon}$ of the nonsmooth objective $\Psi_{\Theta, \gamma}$, and we can apply a gradient descent step to update our approximation to the solution of (1). In our algorithm, the smoothing level ε is automatically reduced and tends to 0, such that the surrogate approaches the original nonsmooth regularizers in (1). More precisely, let $\mathbf{X} = \{\mathbf{x}_1, \mathbf{x}_2, \mathbf{x}_3\}$ for notation simplicity, then we solve the problem $\min_{\mathbf{X}} \Psi_{\Theta, \gamma}(\mathbf{X})$ with initial $\mathbf{X}^{(0)}$ using Algorithm 1 (the initial $\mathbf{X}^{(0)}$ is obtained from a pre-trained initial network, which is illustrated in detail in Section 3.1). At Line 3 of Algorithm 1, we compute a gradient descent update with step size obtained by line search while the smoothing parameter $\varepsilon_t > 0$ is fixed. In Line 4, the algorithm updates ε_t based on a reduction criterion. The reduction of ε_t ensures that the specified subsequence (the subsequence who met the ε_t reduction criterion) must have an accumulation point that is a Clarke stationary point [4] of the optimization problem (1), as given in Theorem 1, whose proof is provided in Supplementary Materials. We create a multi-phase network whose architecture exactly follows Algorithm 1 with a prescribed phase number \hat{T} , where each phase of the network performs one iteration of the algorithm.

Theorem 1. *Suppose that $\{\mathbf{X}^{(t)}\}$ is the sequence generated by Algorithm 1 with any initial $\mathbf{X}^{(0)}$, $\epsilon_{\text{tol}} = 0$ and $T = \infty$. Let $\{\mathbf{X}^{(t_i+1)}\}$ be the subsequence that satisfies the reduction criterion in step 4 of Algorithm 1. Then $\{\mathbf{X}^{(t_i+1)}\}$ has at least one accumulation point, and every accumulation point of $\{\mathbf{X}^{(t_i+1)}\}$ is a Clarke stationary point of $\min_{\mathbf{X}} \Psi_{\Theta, \gamma}(\mathbf{X})$.*

2.3 Bilevel Optimization Algorithm for Network Training

Suppose that we randomly sample \mathcal{M}_{tr} data pairs $\{\mathcal{D}_i^{tr}\}_{i=1}^{\mathcal{M}_{tr}}$ for training and \mathcal{M}_{val} data pairs $\{\mathcal{D}_i^{val}\}_{i=1}^{\mathcal{M}_{val}}$ for validation, where each \mathcal{D}_i^{tr} (or \mathcal{D}_i^{val}) is composed of data pair $\{(\mathbf{f}_1^i, \mathbf{f}_2^i), \mathbf{X}^{*i}\}$, $\mathbf{f}_1^i, \mathbf{f}_2^i$ denote the given partial k-space data, and $\mathbf{X}^{*i} = \{\mathbf{x}_1^{*i}, \mathbf{x}_2^{*i}, \mathbf{x}_3^{*i}\}$ denotes the corresponding reference images.

To find the optimal value of the important hyper-parameter γ for the synthesis term in (1), we employ a bilevel optimization framework which solves for Θ on training set for any given γ in the lower-level problem and tunes the optimal

hyper-parameter γ on validation set in the upper-level problem. More precisely, our bilevel optimization framework reads as:

$$\min_{\Theta, \gamma} \sum_{i=1}^{\mathcal{M}_{val}} \ell(\Theta(\gamma), \gamma; \mathcal{D}_i^{val}) \quad \text{s.t.} \quad \Theta(\gamma) = \arg \min_{\Theta} \sum_{i=1}^{\mathcal{M}_{tr}} \ell(\Theta, \gamma; \mathcal{D}_i^{tr}), \quad (2)$$

$$\begin{aligned} \text{where} \quad \ell(\Theta, \gamma; \mathcal{D}_i) &:= \frac{\mu}{2} \|g_{\theta}([h_{w_1}(\mathbf{x}_1^{*i}), h_{w_2}(\mathbf{x}_2^{*i})]) - \mathbf{x}_3^{*i}\|_2^2 \\ &+ \sum_{j=1}^3 \left(\frac{1}{2} \|\mathbf{x}_j^{(\hat{T})}(\Theta, \gamma; \mathcal{D}_i) - \mathbf{x}_j^{*i}\|_2^2 + (1 - SSIM(\mathbf{x}_j^{(\hat{T})}(\Theta, \gamma; \mathcal{D}_i), \mathbf{x}_j^{*i})) \right), \end{aligned} \quad (3)$$

and the $\mathbf{x}_j^{(\hat{T})}(\cdot)$ denotes the output of the \hat{T} -phase network for the j th modality. The first term of the loss function ℓ in (3) presses g_{θ} to accurately synthesize \mathbf{x}_3 . The second term is to minimize the difference between the network output and the ground truth in the least square sense. The third term is to promote high structural similarity index [21] of the reconstructed/synthesized images. In (2), the lower-level optimization learns the network parameters Θ with any fixed coefficient γ on the training set, and the upper-level tunes the hyper-parameter γ on the validation set, which mitigates the challenging overfitting issue.

The bi-level optimization problem (2) is very difficult to solve. In this work, we employ the penalty method proposed in [13] to solve this problem. For notation simplicity, we denote $\mathcal{L}(\Theta, \gamma; \mathcal{D}) := \sum_{i=1}^{\mathcal{M}} \ell(\Theta, \gamma; \mathcal{D}_i)$ then rewrite (2) as

$$\min_{\Theta, \gamma} \mathcal{L}(\Theta(\gamma), \gamma; \mathcal{D}^{val}) \quad \text{s.t.} \quad \Theta(\gamma) = \arg \min_{\Theta} \mathcal{L}(\Theta, \gamma; \mathcal{D}^{tr}). \quad (4)$$

Following [13], we relax the lower-level optimization problem to its first-order necessary condition:

$$\min_{\Theta, \gamma} \mathcal{L}(\Theta(\gamma), \gamma; \mathcal{D}^{val}) \quad \text{s.t.} \quad \nabla_{\Theta} \mathcal{L}(\Theta, \gamma; \mathcal{D}^{tr}) = 0. \quad (5)$$

Furthermore, we impose a quadratic penalty on the constraint and further relax the above problem as

$$\min_{\Theta, \gamma} \left\{ \tilde{\mathcal{L}}(\Theta, \gamma; \mathcal{D}^{tr}, \mathcal{D}^{val}) := \mathcal{L}(\Theta, \gamma; \mathcal{D}^{val}) + \frac{\lambda}{2} \|\nabla_{\Theta} \mathcal{L}(\Theta, \gamma; \mathcal{D}^{tr})\|^2 \right\}. \quad (6)$$

Due to the large volume of the datasets, it is not possible to solve (6) in full-batch. Here we train the parameters using the mini-batch stochastic alternating direction method summarized in Algorithm 2.

3 Experiments

3.1 Initialization Networks

The initials $\{\mathbf{x}_1^{(0)}, \mathbf{x}_2^{(0)}, \mathbf{x}_3^{(0)}\}$ are obtained through the Initialization Networks (INIT-Nets) shown in Fig. 1, where the **k-space interpolation block** interpolates the missing components of the undersampled k-space data then fed into

Algorithm 2: Mini-batch alternating direction penalty algorithm

```

1: Input  $\mathcal{D}^{tr}, \mathcal{D}^{val}, \delta_{tol} > 0$ , Initialize  $\Theta, \gamma, \delta, \lambda > 0$  and  $\nu_\delta \in (0, 1), \nu_\lambda > 1$ .
2: while  $\delta > \delta_{tol}$  do
3:   Sample training and validation batch  $\mathcal{B}^{tr} \subset \mathcal{D}^{tr}, \mathcal{B}^{val} \subset \mathcal{D}^{val}$ .
4:   while  $\|\nabla_\Theta \tilde{\mathcal{L}}(\Theta, \gamma; \mathcal{B}^{tr}, \mathcal{B}^{val})\|^2 + \|\nabla_\gamma \tilde{\mathcal{L}}(\Theta, \gamma; \mathcal{B}^{tr}, \mathcal{B}^{val})\|^2 > \delta$  do
5:     for  $k = 1, 2, \dots, K$  (inner loop) do
6:        $\Theta \leftarrow \Theta - \rho_\Theta^{(k)} \nabla_\Theta \tilde{\mathcal{L}}(\Theta, \gamma; \mathcal{B}^{tr}, \mathcal{B}^{val})$ 
7:     end for
8:      $\gamma \leftarrow \gamma - \rho_\gamma \nabla_\gamma \tilde{\mathcal{L}}(\Theta, \gamma; \mathcal{B}^{tr}, \mathcal{B}^{val})$ 
9:   end while and update  $\delta \leftarrow \nu_\delta \delta, \lambda \leftarrow \nu_\lambda \lambda$ .
10: end while and output:  $\Theta, \gamma$ .

```

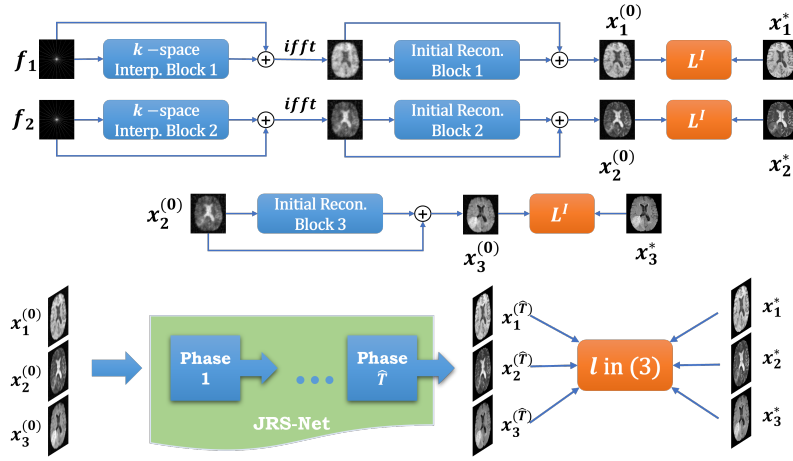


Fig. 1: The overall architecture of the proposed network for joint multimodal MRI reconstruction and synthesis: INIT-Nets (up and middle), JRS-Net (bottom).

the **initial reconstruction block** in the image domain after inverse Fourier transform. All blocks are designed in residual structure [8]. To train the INIT-Nets, we minimize the difference between its outputs and the ground truth with loss $L^I(\mathbf{x}_j^{(0)}, \mathbf{x}_j^*) = \|\mathbf{x}_j^{(0)} - \mathbf{x}_j^*\|_1$, $j = 1, 2, 3$. The INIT-Nets only produce initial approximate images with limited accuracy, so we fed them into the Joint Reconstruction and Synthesis Network (JRS-Net) illustrated in Section 2.2 to obtain the final results. INIT-Nets are pre-trained whose parameters are fixed during training the JRS-Net.

3.2 Experiment Setup

The datasets are from BRATS 2018 challenge [14] which were scanned from four modalities T1, T2, Flair and T1-weighted contrast-enhanced (T1CE) and we picked high-grade gliomas (HGG) set which consists 210 patients. We randomly

Table 1: Quantitative comparison of the synthesis results.

	Methods	PSNR	SSIM	NMSE
T1 + T2 \rightarrow FLAIR	MM [3]	22.89 \pm 1.48	0.6671 \pm 0.0586	0.0693 \pm 0.0494
	MM-GAN [17]	23.35 \pm 1.03	0.7084 \pm 0.0370	0.0620 \pm 0.0426
	MMGradAdv [12]	24.03 \pm 1.40	0.7586 \pm 0.0326	0.0583 \pm 0.0380
	Hi-Net [27]	25.03 \pm 1.38	0.8499 \pm 0.0300	0.0254 \pm 0.0097
	Proposed	26.19\pm1.34	0.8677\pm0.0307	0.0205\pm0.0087
$\mathbf{f}_{T1} + \mathbf{f}_{T2} \rightarrow$ FLAIR	Proposed	25.74\pm1.25	0.8597\pm0.0315	0.0215\pm0.0085
T1 + FLAIR \rightarrow T2	MM [3]	23.89 \pm 1.61	0.6895 \pm 0.0511	0.0494 \pm 0.0185
	MM-GAN [17]	24.15 \pm 0.90	0.7217 \pm 0.0432	0.0431 \pm 0.0114
	MMGradAdv [12]	25.06 \pm 1.49	0.7597 \pm 0.0486	0.0406 \pm 0.0165
	Hi-Net [27]	25.95 \pm 1.50	0.8552 \pm 0.0410	0.0229 \pm 0.0070
$\mathbf{f}_{T1} + \mathbf{f}_{FLAIR} \rightarrow$ T2	Proposed	26.52\pm1.57	0.8610\pm0.0438	0.0207\pm0.0072
T2 + FLAIR \rightarrow T1	MM [3]	23.53 \pm 2.18	0.7825 \pm 0.0470	0.0301 \pm 0.0149
	MM-GAN [17]	23.63 \pm 2.31	0.7908 \pm 0.0421	0.0293 \pm 0.0119
	MMGradAdv [12]	24.73 \pm 2.23	0.8065 \pm 0.0423	0.0252 \pm 0.0118
	Hi-Net [27]	25.64 \pm 1.59	0.8729 \pm 0.0349	0.0130 \pm 0.0097
$\mathbf{f}_{T2} + \mathbf{f}_{FLAIR} \rightarrow$ T1	Proposed	26.31\pm1.80	0.9085\pm0.0311	0.0112\pm0.0113
T1 + T2 \rightarrow T1CE	MM [3]	23.37 \pm 1.56	0.7272 \pm 0.0574	0.0312 \pm 0.0138
	MM-GAN [17]	23.68 \pm 0.97	0.7577 \pm 0.0637	0.0302 \pm 0.0133
	MMGradAdv [12]	24.23 \pm 1.90	0.7887 \pm 0.0519	0.0273 \pm 0.0136
	Hi-Net [27]	25.21 \pm 1.20	0.8650 \pm 0.0328	0.0180 \pm 0.0134
$\mathbf{f}_{T1} + \mathbf{f}_{T2} \rightarrow$ T1CE	Proposed	25.91\pm1.21	0.8726\pm0.0340	0.0167\pm0.0133

Table 2: Quantitative comparison of the reconstructed T1 and T2 images without and with joint synthesis of FLAIR images.

Modality	FLAIR involved?	PSNR	SSIM	NMSE
T1	No	37.00 \pm 0.74	0.9605 \pm 0.0047	0.0008 \pm 0.0002
	Yes	37.49 \pm 0.83	0.9628 \pm 0.0074	0.0007 \pm 0.0002
T2	No	37.24 \pm 1.22	0.9678 \pm 0.0028	0.0027 \pm 0.0010
	Yes	37.67 \pm 1.34	0.9663 \pm 0.0043	0.0024 \pm 0.0009

took the center 10 slices from 6 patients as test set with cropped size 160×180 and split the rest of HGG dataset into training and validation sets with 1020 images separately. We compared with four state-of-the-art multimodal MR synthesis methods: Multimodal MR (MM) [3], MM-GAN [17], MMGradAdv [12] and Hi-Net [27]. The inputs for our method are the partial k-space data scanned with a radial mask with sampling ratio 40%. The hyper-parameter selection for our algorithm is provided in Supplementary Material. Three metrics are used for evaluation: peak signal-to-noise ratio (PSNR) [9], structural similarity (SSIM) [21], and normalized mean squared error (NMSE) [16].

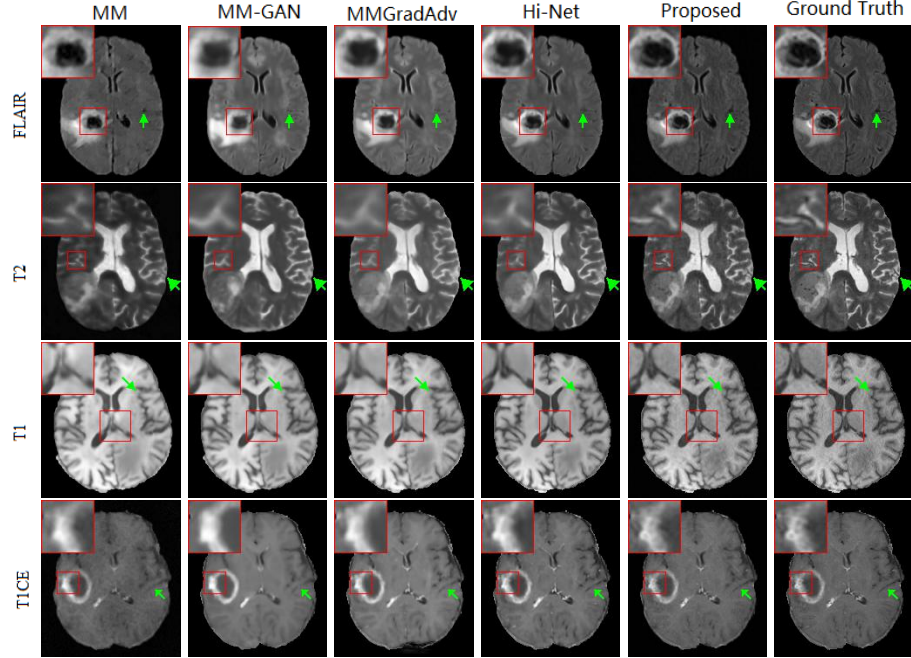


Fig. 2: Qualitative comparison between the state-of-the-art multimodal synthesis methods and proposed method. From first row to last row: T1 + T2 \rightarrow FLAIR, T1 + FLAIR \rightarrow T2, T2 + FLAIR \rightarrow T1 and T1 + T2 \rightarrow T1CE.

3.3 Experimental Results and Evaluation

We take four synthesis directions T1 + T2 \rightarrow FLAIR, T1 + FLAIR \rightarrow T2, T2 + FLAIR \rightarrow T1 and T1 + T2 \rightarrow T1CE. Table 1 reports the quantitative result, which indicates that the proposed method outperforms MM and GAN-based methods (MM-GAN, MMGradAdv, Hi-Net). The average PSNR of our method improves 0.67 dB comparing to the baseline Hi-Net, SSIM improves about 0.01, and NMSE reduces about 0.01. We also conduct the pure-synthesis experiment (T1 + T2 \rightarrow FLAIR) by inputting fully-scanned source data, where the model (1) minimizes w.r.t. \mathbf{x}_3 only and excludes the data-fidelity terms. This result is in Table 1 where the PSNR value is 1.16 dB higher than baseline method Hi-Net. Table 2 shows that the joint reconstruction and synthesis improves PSNR by 0.46 dB comparing to purely reconstructing T1 and T2 without synthesizing FLAIR. We think this is because that the synthesis operator g_θ also leverages data \mathbf{x}_3 to assist shaping the feature maps of \mathbf{x}_1 and \mathbf{x}_2 , which improves the reconstruction quality of the latter images.

Fig. 2 displays the synthetic MRI results on different source and target modality images. The proposed synthetic images preserve more details and distinct edges of the tissue boundary (indicated by the magnified red windows

and green arrows) and the synthetic images are more alike the ground truth images comparing to other referenced methods.

4 Conclusion

We propose a novel deep model that simultaneously reconstructs the source modality images from the partially scanned k-space MR data and synthesizes the target modality image without any k-space information by iterating an LOA with convergence guaranteed. The network is trained by a bilevel-optimization training algorithm that uses training and validation sets to further improve the performance. Extensive experiments on brain MR data with different modalities validate the magnificent performance of the proposed model.

References

1. Bian, W., Chen, Y., Ye, X.: An optimal control framework for joint-channel parallel mri reconstruction without coil sensitivities. *Magnetic Resonance Imaging* (2022)
2. Bian, W., Chen, Y., Ye, X., Zhang, Q.: An optimization-based meta-learning model for mri reconstruction with diverse dataset. *Journal of Imaging* **7**(11) (2021)
3. Chatsias, A., Joyce, T., Giuffrida, M.V., Tsiftaris, S.A.: Multimodal mr synthesis via modality-invariant latent representation. *IEEE transactions on medical imaging* **37**(3), 803–814 (2017)
4. Chen, Y., Liu, H., Ye, X., Zhang, Q.: Learnable descent algorithm for nonsmooth nonconvex image reconstruction. *SIAM Journal on Imaging Sciences* **14**(4), 1532–1564 (2021)
5. Cheng, J., Wang, H., Ying, L., Liang, D.: Model learning: Primal dual networks for fast mr imaging. In: *International Conference on Medical Image Computing and Computer-Assisted Intervention*. pp. 21–29. Springer (2019)
6. Dar, S.U., Yurt, M., Karacan, L., Erdem, A., Erdem, E., Çukur, T.: Image synthesis in multi-contrast mri with conditional generative adversarial networks. *IEEE transactions on medical imaging* **38**(10), 2375–2388 (2019)
7. Dar, S.U., Yurt, M., Shahdloo, M., Ildiz, M.E., Tınaz, B., Çukur, T.: Prior-guided image reconstruction for accelerated multi-contrast mri via generative adversarial networks. *IEEE Journal of Selected Topics in Signal Processing* **14**(6), 1072–1087 (2020)
8. He, K., Zhang, X., Ren, S., Sun, J.: Deep residual learning for image recognition. In: *Proceedings of the IEEE conference on computer vision and pattern recognition*. pp. 770–778 (2016)
9. Hore, A., Ziou, D.: Image quality metrics: Psnr vs. ssim. In: *2010 20th international conference on pattern recognition*. pp. 2366–2369. IEEE (2010)
10. Iglesias, J.E., Konukoglu, E., Zikic, D., Glocker, B., Van Leemput, K., Fischl, B.: Is synthesizing mri contrast useful for inter-modality analysis? In: *International Conference on Medical Image Computing and Computer-Assisted Intervention*. pp. 631–638. Springer (2013)
11. Lee, D., Yoo, J., Tak, S., Ye, J.C.: Deep residual learning for accelerated mri using magnitude and phase networks. *IEEE Transactions on Biomedical Engineering* **65**(9), 1985–1995 (2018)

12. Liu, X., Yu, A., Wei, X., Pan, Z., Tang, J.: Multimodal mr image synthesis using gradient prior and adversarial learning. *IEEE Journal of Selected Topics in Signal Processing* **14**(6), 1176–1188 (2020)
13. Mehra, A., Hamm, J.: Penalty method for inversion-free deep bilevel optimization. *arXiv preprint arXiv:1911.03432* (2019)
14. Menze, B.H., Jakab, A., Bauer, S., Kalpathy-Cramer, J., Farahani, K., Kirby, J., Burren, Y., Porz, N., Slotboom, J., Wiest, R., et al.: The multimodal brain tumor image segmentation benchmark (brats). *IEEE transactions on medical imaging* **34**(10), 1993–2024 (2014)
15. Monga, V., Li, Y., Eldar, Y.C.: Algorithm unrolling: Interpretable, efficient deep learning for signal and image processing. *IEEE Signal Processing Magazine* **38**(2), 18–44 (2021)
16. Poli, A., Cirillo, M.: On the use of the normalized mean square error in evaluating dispersion model performance. *Atmospheric Environment. Part A. General Topics* **27**, 2427–2434 (10 1993)
17. Sharma, A., Hamarneh, G.: Missing mri pulse sequence synthesis using multi-modal generative adversarial network. *IEEE transactions on medical imaging* **39**(4), 1170–1183 (2019)
18. Sohail, M., Riaz, M.N., Wu, J., Long, C., Li, S.: Unpaired multi-contrast mr image synthesis using generative adversarial networks. In: *International Workshop on Simulation and Synthesis in Medical Imaging*. pp. 22–31. Springer (2019)
19. Sriram, A., Zbontar, J., Murrell, T., Defazio, A., Zitnick, C.L., Yakubova, N., Knoll, F., Johnson, P.: End-to-end variational networks for accelerated mri reconstruction. In: *International Conference on Medical Image Computing and Computer-Assisted Intervention*. pp. 64–73. Springer (2020)
20. Sun, J., Li, H., Xu, Z., et al.: Deep admn-net for compressive sensing mri. *Advances in neural information processing systems* **29** (2016)
21. Wang, Z., et al.: Image quality assessment: from error visibility to structural similarity. *IEEE transactions on image processing* **13**(4), 600–612 (2004)
22. Welander, P., Karlsson, S., Eklund, A.: Generative adversarial networks for image-to-image translation on multi-contrast mr images-a comparison of cyclegan and unit. *arXiv preprint arXiv:1806.07777* (2018)
23. Yang, G., Yu, S., Dong, H., Slabaugh, G., Dragotti, P.L., Ye, X., Liu, F., Arridge, S., Keegan, J., Guo, Y., et al.: Dagan: Deep de-aliasing generative adversarial networks for fast compressed sensing mri reconstruction. *IEEE transactions on medical imaging* **37**(6), 1310–1321 (2017)
24. Yang, Y., Wang, N., Yang, H., Sun, J., Xu, Z.: Model-driven deep attention network for ultra-fast compressive sensing mri guided by cross-contrast mr image. In: *International Conference on Medical Image Computing and Computer-Assisted Intervention*. pp. 188–198. Springer (2020)
25. Yurt, M., Dar, S.U., Erdem, A., Erdem, E., Oguz, K.K., Çukur, T.: Mustgan: Multi-stream generative adversarial networks for mr image synthesis. *Medical Image Analysis* **70**, 101944 (2021)
26. Zhang, J., Ghanem, B.: Ista-net: Interpretable optimization-inspired deep network for image compressive sensing. In: *Proceedings of the IEEE conference on computer vision and pattern recognition*. pp. 1828–1837 (2018)
27. Zhou, T., Fu, H., Chen, G., Shen, J., Shao, L.: Hi-net: hybrid-fusion network for multi-modal mr image synthesis. *IEEE transactions on medical imaging* **39**(9), 2772–2781 (2020)

1 Proof of Theorem 1

We assume that $\Psi_{\Theta,\gamma}$ is coercive and $\Psi_{\Theta,\gamma}^* = \min_{\mathbf{X}} \Psi_{\Theta,\gamma}(\mathbf{X}) > -\infty$, which are easy to satisfy in practice. For any set $\mathcal{S} \subset \mathbb{R}^n$, we denote $\text{dist}(\mathbf{y}, \mathcal{S}) := \inf\{\|\mathbf{y} - \mathbf{x}\| \mid \mathbf{x} \in \mathcal{S}\}$. The definition of the Clark subdifferential and Clark stationary point can be found in [4]. We need the following lemmas to prove Theorem 1. Since Lemma 2 can be verified by direct calculation, and Lemma 3 and 4 are similar as those given in [4,2], we omit their proofs here.

Lemma 1. *The gradient of $\Psi_{\Theta,\gamma}^\varepsilon(\mathbf{X})$ is Lipschitz continuous.*

Proof. Notice that $\Psi_{\Theta,\gamma}^\varepsilon(\mathbf{X})$ is the smoothing surrogate of the $\Psi_{\Theta,\gamma}(\mathbf{X})$ in (1) with $\|h_{w_i}(\mathbf{x}_i)\|_{2,1}$ replaced by $\|h_{w_i}(\mathbf{x}_i)\|_{\varepsilon_{2,1}}$ in the second sum. As both h_{w_i} and g_θ are compositions of Lipschitz continuous, we know the first and last terms of $\Psi_{\Theta,\gamma}^\varepsilon(\mathbf{X})$ are Lipschitz continuous. The second sum is Lipschitz continuous proved by the Lemma A2 in [2].

Lemma 2. *For any $\varepsilon > 0$, $\|h_{w_i}(\mathbf{x}_i)\|_{\varepsilon_{2,1}} \leq \|h_{w_i}(\mathbf{x}_i)\|_{2,1} \leq \|h_{w_i}(\mathbf{x}_i)\|_{\varepsilon_{2,1}} + m\varepsilon$.*

Lemma 3. *Suppose the sequence $\{\mathbf{X}^{(t)}\}$ is generated by executing Lines 3 of Algorithm 1 with fixed $\varepsilon_t = \varepsilon$ then*

1. $\|\nabla \Psi_{\Theta,\gamma}^\varepsilon(\mathbf{X}^{(t)})\| \rightarrow 0$ as $t \rightarrow \infty$.
2. *The condition in Step 4 of Algorithm 1 for reducing ε can be met in finite iterations.*

Lemma 4. *Suppose the sequence $\{\mathbf{X}^{(t)}\}$ is generated by Algorithm 1 with initial $\mathbf{X}^{(0)}$, then we have $\Psi_{\Theta,\gamma}^{\varepsilon_{t+1}}(\mathbf{X}^{(t+1)}) + m\varepsilon_{t+1} \leq \Psi_{\Theta,\gamma}^{\varepsilon_t}(\mathbf{X}^{(t)}) + m\varepsilon_t$ for any $t \geq 0$.*

The proof of **Theorem 1** is outlined below.

Proof (Theorem 1). From Lemma 2, we have $\Psi_{\Theta,\gamma}(\mathbf{X}) \leq \Psi_{\Theta,\gamma}^\varepsilon(\mathbf{X}) + m\varepsilon$ for any $\varepsilon > 0$. Together with Lemma 4, we get $\Psi_{\Theta,\gamma}(\mathbf{X}^{(t)}) \leq \Psi_{\Theta,\gamma}^{\varepsilon_t}(\mathbf{X}^{(t)}) + m\varepsilon_t \leq \dots \leq \Psi_{\Theta,\gamma}^{\varepsilon_0}(\mathbf{X}^{(0)}) + m\varepsilon_0 < \infty$. As $\Psi_{\Theta,\gamma}$ is coercive, we know that $\{\mathbf{X}^{(t)}\}$ is bounded. Let $\mathbf{X}^{(t_l+1)}$ denote the l -th $\mathbf{X}^{(t)}$ that satisfies the reduction criterion in step 4 of Algorithm 1. Then we can partition the whole sequence $\{\mathbf{X}^{(t)}\}$ into segments correspondingly such that the associated $\varepsilon_t = \varepsilon_{t_l+1} = \varepsilon_0 \eta^l$ for $t = t_l + 1, \dots, t_{l+1}$ in the l -th segment, and the length of each segment is bounded according to Lemma 3.m, As $\mathbf{X}^{(t_l+1)}$ satisfies the reduction criterion in step 4 of Algorithm 1, we have $\|\nabla \Psi_{\Theta,\gamma}^{\varepsilon_{t_l}}(\mathbf{X}^{(t_l+1)})\| \leq \sigma \varepsilon_{t_l} \eta = \sigma \varepsilon_0 \eta^{l+1} \rightarrow 0$ as $l \rightarrow \infty$. Then, there exists at least one convergent subsequence of $\mathbf{X}^{(t_l+1)}$, dubbed $\{\mathbf{X}^{(k+1)}\}$, and a point $\hat{\mathbf{X}}$ that satisfies $\mathbf{X}^{(k+1)} \rightarrow \hat{\mathbf{X}}$, $\varepsilon_k \rightarrow 0$, and $\nabla \Psi_{\Theta,\gamma}^{\varepsilon_k}(\mathbf{X}^{(k+1)}) \rightarrow 0$ as $k \rightarrow \infty$, where ε_k is the corresponding ε_{t_l} associated with $\mathbf{X}^{(k+1)}$. Denote $\mathbf{X} = \{\mathbf{x}_1, \mathbf{x}_2, \mathbf{x}_3\}$. The Clark subdifferential of each \mathbf{x}_i is identical to [2] except for an additional smooth term in (1), so the analysis for each individual \mathbf{x}_i is the same as [2]. It has been proved in [2] that $\text{dist}(\nabla \Psi_{\Theta,\gamma}^{\varepsilon_k}(\mathbf{x}_i^{(k+1)}), \partial^C \Psi_{\Theta,\gamma}(\hat{\mathbf{x}}_i)) \rightarrow 0$, as $k \rightarrow \infty$, where ∂^C denotes the Clark subdifferential. As this holds for each \mathbf{x}_i , then we can get it also holds for \mathbf{X} that $\text{dist}(\nabla \Psi_{\Theta,\gamma}^{\varepsilon_k}(\mathbf{X}^{(k+1)}), \partial^C \Psi_{\Theta,\gamma}(\hat{\mathbf{X}})) \rightarrow 0$, as $k \rightarrow \infty$. Since $\nabla \Psi_{\Theta,\gamma}^{\varepsilon_k}(\mathbf{X}^{(k+1)}) \rightarrow 0$ and $\partial^C \Psi_{\Theta,\gamma}(\hat{\mathbf{X}})$ is closed, we conclude that $0 \in \partial^C \Psi_{\Theta,\gamma}(\hat{\mathbf{X}})$.

Table 1: The hyper-parameter selection. The parameters for Algorithm 1 are determined after trials by considering both algorithm convergence and the computational efficiency. The batch size is determined due to the consideration of the GPU (Nvidia GTX-1080Ti) memory and the data volume. For Algorithm 2, the selection of δ_{tol} makes the algorithm stop at around 1000 epochs.

Initializer	Xavier [8]	l	4	η	0.5	ϵ_{tol}	1×10^{-3}
Optimizer	ADAM [12]	kernel of h_{w_i}	$3 \times 3 \times 64$	ε_0	0.001	ν_δ	0.95
Learning Rate	0.001	l'	6	a	10^5	δ	1×10^{-3}
batch size	2	kernel of g_θ	$3 \times 3 \times 128$	σ	10^3	λ	1×10^{-4}
μ	0.1	α_0	0.01	T	11	ν_λ	1.001
γ	1	$\rho_\Theta^{(0)}$	0.9	δ_{tol}	4.35×10^{-6}	ρ_γ	0.9

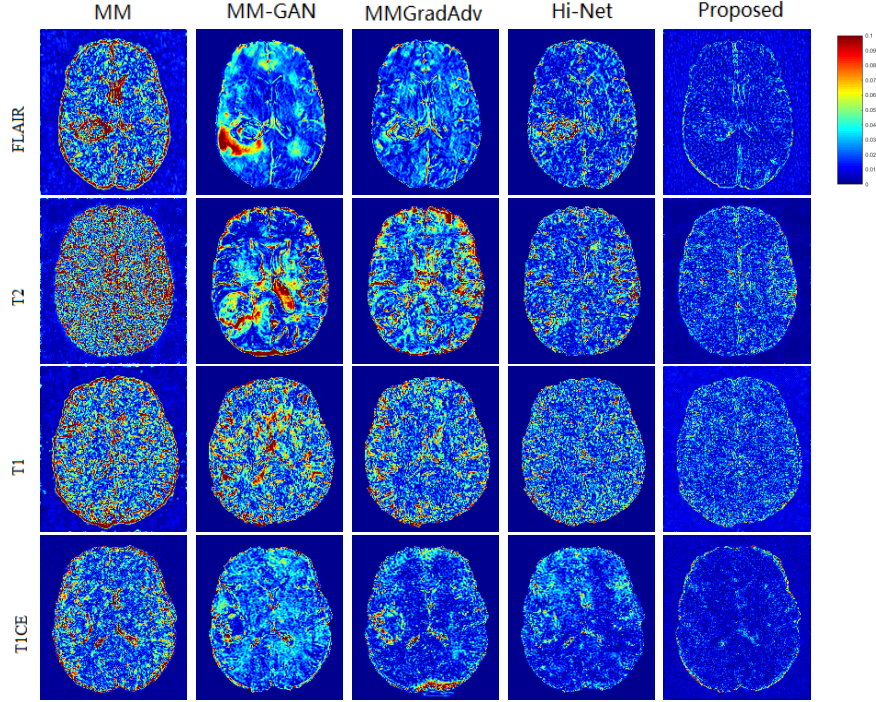


Fig. 1: Pointwise error maps between synthetic image and the its corresponding ground truth. From first row to last row: T1 + T2 \rightarrow FLAIR, T1 + FLAIR \rightarrow T2, T2 + FLAIR \rightarrow T1 and T1 + T2 \rightarrow T1CE.